



UKAEA-CCFE-PR(25)378

P. Srinivasan, M. R. Gilbert, S. Puri, K. P. Dominguez, A. Horsfield, D. Nguyen-Manh

An Atomic Cluster Expansion interatomic potential for lithium: investigating the solid and liquid phases

Enquiries about copyright and reproduction should in the first instance be addressed to the UKAEA Publications Officer, Culham Science Centre, Building K1/0/83 Abingdon, Oxfordshire, OX14 3DB, UK. The United Kingdom Atomic Energy Authority is the copyright holder.
The contents of this document and all other UKAEA Preprints, Reports and Conference Papers are available to view online free at scientific-publications.ukaea.uk/

An Atomic Cluster Expansion interatomic potential for lithium: investigating the solid and liquid phases

P. Srinivasan, M. R. Gilbert, S. Puri, K. P. Dominguez, A. Horsfield, D. Nguyen-Manh

An Atomic Cluster Expansion interatomic potential for lithium: investigating the solid and liquid phases

Prashanth Srinivasan* and Mark R. Gilbert United Kingdom Atomic Energy Authority, Culham Campus , Abingdon, OX14 3DB, UK

Siddharth Puri and Karen Pacho Dominguez Department of Materials, Imperial College London, South Kensington Campus, London SW7 2AZ, U.K.

Andrew Horsfield

Department of Materials, Imperial College London, South Kensington Campus, London SW7 2AZ, U.K. and United Kingdom Atomic Energy Authority, Culham Campus, Abingdon, OX14 3DB, UK

Duc Nguyen-Manh

United Kingdom Atomic Energy Authority, Culham Campus, Abingdon, OX14 3DB, UK and Department of Materials, University of Oxford, OX10 3PH, UK (Dated: December 24, 2024)

We develop an atomic cluster expansion (ACE) interatomic potential for lithium that accurately models both the solid and liquid phase and the corresponding melting point. The predicted properties for both phases are in close agreement with density functional theory (DFT) and experimental data from literature. The potential is able to capture the energy differences of the different competing phases of the solid at 0 K. It also predicts temperature dependent liquid density, viscosity, and diffusion coefficient. The melting point is calculated using the two-phase coexistence method. By using the ACE formalism, we also systematically investigate the contributions of different N-body interactions and the number of radial parameters needed to separately represent both phases, thereby shedding light on the complexity of the ACE potential needed to model solid and liquid lithium efficiently.

I. INTRODUCTION

In order to design and build sustainable fusion reactors, it is important to understand the behavior of lithium and lithium-based compounds. Liquid lithium, eutectic liquid lithium-lead alloy, solid lithium ceramics and lithium-based salts have been touted as prime candidates for tritium breeding [1, 2]. An additional advantage of liquid Lithium is the possibility to use it as a coolant by absorbing the heat coming from the high neutron flux [3]. After operation, the breeder gets quenched down to cryogenic temperature, and liquid breeder materials solidify in this process. Hence, it becomes crucial to understand the temperature dependent behavior of both solid and liquid Lithium phases under external conditions.

Several questions remain unanswered regarding the use of lithium as a breeder, and the storage and diffusion of hydrogen isotopes within the breeder. Experimental understanding is possible, albeit very expensive and difficult. Computational techniques such as atomistic simulations provide a safe and flexible way to analyze and fundamentally understand such systems under different conditions. The reliability of the results, however, is dependent on the accuracy of the interatomic potential that

drives the dynamics of the system. One also needs a computationally affordable potential that can be scaled to bigger system sizes.

Lithium has only been partially investigated in literature using atomistic simulation techniques, owing to the lack of accurate interatomic potentials that span both the solid and liquid phase. The phase diagram of solid Li across the temperature-pressure range is quite complex [4–6]. First principles density functional theory (DFT) predicts several energetically competing phases at 0 K with the face-centered cubic (FCC) as the lowestenergy structure [7], and body-centered cubic (bcc), hexagonal close-packed (hcp) and rhombohedral h9R structures only marginally higher in energy compared to the fcc phase [8]. However, the bcc phase becomes entropically stabilized already at 100 K-200 K, making it the experimentally observed room-temperature phase [8– 10]. Accurately capturing these tiny energy differences in an interatomic potential becomes very challenging. Nichol et al. [11] developed an EAM potential to study property trends in simple metals, including Li. In order to also include angular terms in the formalism, Ko et al. [12] and Qin et al. [13] developed second-nearest neighbor modified embedded atom method (2NN-MEAM) potentials for predicting phase transitions in solid Li. Besides empirical potentials, Phuthi et al. [14], Zuo et al. [15] and Wang et al. [16] trained machine-learning based interatomic potentials (MLIPs) to study bulk and

^{*} prashanth.srinivasan@ukaea.uk

surface properties of solid Li, and high-pressure structures of solid Li, respectively. While all the above potentials predict the overall behavior of solid Li quite accurately, there are always certain properties that are more challenging to capture. For instance, some of the potentials fail to capture the bcc-fcc-9R energy difference, or accurate elastic constants of bcc and fcc phases. Nevertheless, none of the potentials have explicitly been developed or trained to model liquid Li.

There has been even fewer attempts at developing an interatomic potential to model the liquid phase of lithium. In 2009, Belashchenko et al. [17] developed an embedded atom method (EAM) interatomic potential by fitting to experimental data above melting point. Cui et al., [18] developed a more improved second nearest neighbor modified embedded atom method (2NN-MEAM) potential which outperformed the EAM in accuracy. Both these potentials were unable to predict accurate values of the temperature-dependent viscosity and self-diffusion coefficient. More recently, Al-Awad et al., [19] developed an EAM potential that rectified these drawbacks. By introducing a long range oscillatory form of the pair potential, they were able to tune the potential to the experimental melting point and experimental densities, and ultimately achieve other properties more accurately. The applicability of the above potentials is however restricted only to the liquid phase.

To capture both the solid and liquid phase accurately, a more complex functional form of the local atomic environment descriptor is required than what empirical potentials such as the EAM and the 2NN-MEAM offer. MLIPs provide us with this flexibility to model more complex atomic systems since they are derived from complex local atomic environment descriptors and hence a larger parameter space. Several classes of MLIPs have garnered attention over the last two decades, each with their own sets of descriptors [20–30]. One such machinelearning based model is the atomic cluster expansion (ACE) interatomic potential [31]. The ACE potential provides a complete and efficient representation of properties as a function of local atomic environment using many-body functions. The basis set used to represent atomic structures in the ACE formalism has been proven to be complete in several works in literature [31–33]. Hence, in this work, we develop an ACE MLIP to model the lithium system, by training the potential on ab initio DFT data that includes both the solid and liquid phase.

The developed potential accurately captures the $0\,\mathrm{K}$ energy difference between different crystalline structures, the temperature-dependent mechanical properties of the solid bcc phase, and several properties of liquid lithium. Additionally, it also predicts a melting point that is extremely close to the experimentally known value. The formalism of the ACE potential consists of contributions to the total energy arising from different N-body terms. We analyze the effect of these contributions on solid and liquid lithium properties by also training and comparing a set of ACE potentials that include different many-body

terms. Additionally, we analyze the complexity of the ACE potential that is needed to model both phases by training potentials with different number of parameters.

The manuscript is arranged as follows. The computational details of building the DFT training set, training the ACE potential, and performing molecular dynamics (MD) simulations are provided in Section II. In Section III, we show the results of the final fitted potential on both phases and compare them to DFT and experimental data. In Section IV, we discuss the contribution of many-body terms, and perform a cost-accuracy analysis of a set of potentials trained with different number of radial and angular parameters. The conclusions and outlook of the manuscript are summarized in Section V.

II. COMPUTATIONAL METHODS

A. DFT training data

The ACE potential is trained on first principles calculations based on density functional theory (DFT). All DFT calculations are performed using the VASP code [34] within the projected augmented-wave (PAW) method [35, 36]. For the results shown in the main text, the ACE is trained on DFT data that uses the generalized gradient approximation (GGA) exchange correlation (XC) functional by Perdew, Burke, and Ernzerhof (PBE) [37]. The effect of the XC functional is discussed in the Supplementary Information, where results using the local density approximation (LDA) [38] XC functional are compared to those using GGA. The DFT calculations include one valence electron for Lithium. A Methfessel-Paxton smearing method [39] with a smearing width of 0.1 eV is utilized to approximate the occupation function. The calculations for the training set are performed on 128-atom supercells (modified accordingly for vacancy, interstitial and non-bcc structures) with an energy cut-off of $450\,\mathrm{eV}$ and a $2\times2\times2$ k-point grid. While comparing the ACE predictions of properties to DFT, more strict parameters (550 eV energy cutoff and $4\times4\times4$ k-point grid) are employed.

The training set used to fit the ACE potential contains both solid and liquid configurations obtained from 0 K static DFT and high-temperature ab initio molecular dynamics (AIMD) simulations. To sample the solid phase, we explicitly include 100 0 K structures within a certain volume range, for each of the four energetically competing phases to the training set. We perform AIMD simulations of the bcc, fcc and hcp phases at 400 K for a set of four volumes each. Additionally, we also choose bcc structures with different number of vacancies (one to four), with a < 111 > self-interstitial (which is the most stable self-interstitial atom (SIA) defective structure), and with a [100] and a [110] free surface as initial structures and perform AIMD runs at 400 K. To sample the liquid phase, AIMD simulations are performed at five different temperatures and five volumes at each temperature. All AIMD simulations for both phases are run in the NVT ensemble for 1000 steps with a timestep 0.5 fs. The complete set of calculations is summarized in Table I. In order to obtain uncorrelated snapshots, we pick one in every ten AIMD configurations for training the potential. Overall, the training dataset contains 2500 liquid snapshots and 4200 solid snapshots.

B. Atomic Cluster Expansion interatomic potential - formalism

The energy of a system with N atoms can be represented as a sum of individual atomic energies, given by

$$E_{\text{tot}} = \sum_{i=1}^{N} E_i. \tag{1}$$

Each atomic energy is restricted to within a certain cutoff. This locality of interactions provides a linear scaling with system size. The atomic energies E_i can be obtained from a combination of different atomic properties $\varphi_i^{(p)}$, which could, in principle, represent bonding, repulsion etc. Hence, E_i can generically be expressed as a nonlinear function given as

$$E_i = \mathcal{F}(\varphi_i^{(1)}, \varphi_i^{(2)}, \dots, \varphi_i^{(p)}). \tag{2}$$

In the linear ACE formalism, The atomic energy E_i is directly expressed as

$$E_i = \varphi_i. \tag{3}$$

However, for metallic systems, a faster convergence of the atomic energy with many-body interactions can possibly be achieved by employing a non-linear form representative of the Finnis-Sinclair potential [40], as given by

$$E_i = \varphi_i^{(1)} + \sqrt{\varphi_i^{(2)}},\tag{4}$$

where $\varphi_i^{(1)}$ and $\varphi_i^{(2)}$ are representative of the pairwise repulsion and the embedding function. Each $\varphi_i^{(p)}$ can be expanded within the ACE formalism using a set of atomic descriptors given by

$$\varphi_i^{(p)} = \sum_{v} c_v^{(p)} \boldsymbol{B}_{iv}, \tag{5}$$

where $c_v^{(p)}$ are the expansion coefficients and \boldsymbol{B}_{iv} the basis functions with multi-indices v.

The building blocks for the ACE atomic descriptors are a set of orthogonal and complete single-bond basis functions $\phi_v(r)$, expressed as

$$\phi_{\upsilon}(r) = R_{nl}(r_{ii})Y_{lm}(\hat{\boldsymbol{r}}_{ii}), \tag{6}$$

where R_{nl} are radial functions that depend on the distance from atom i to atom j, Y_{lm} are spherical harmonic

functions depending on the direction \hat{r} , and v=(nlm) is a cumulative index. The complexity of the descriptor can be altered by choosing different values of n and l prior to training the potential. Choosing larger values provides more flexibility tailored towards a more widespread training dataset, but significantly increases the computational cost of using the potential to do MD simulations. The atomic base A, obtained by projecting the local basis functions on the atomic density, is expressed as

$$A_{iv} = \sum_{j} \phi_{v}(\mathbf{r}_{ji}), \tag{7}$$

following which basis functions ${\pmb A}$ of different body-orders ν are constructed as

$$\mathbf{A}_{iv} = \prod_{t=1}^{\nu} A_{iv_t}.$$
 (8)

In Equation 3, with every additional product, an additional term in the N-body decomposition of the atomic property can be parametrized. More specifically, only up to two-body interactions can be parametrized using t=1. To account for three-body interactions, one needs to consider basis functions up to t=2, and up to t=3 for four-body interactions, and so on. The basis functions in Equation 3 need to fulfill symmetries of translation, rotation, inversion and permutation. The above equation gets reformulated as

$$\boldsymbol{B}_{iv} = \sum_{v'} \boldsymbol{C}_{vv'} \boldsymbol{A}_{iv'}, \tag{9}$$

where the generalized Clebsch-Gordan coefficients C remove functions that are not rotationally invariant, leading to the final set of basis functions B_{iv} mentioned previously in Equation 5 in the expansion of any atomic property $\varphi_i^{(p)}$.

In the Discussion section, we study the effect of different many-body interactions (different values of t in Eq. 8) on the ACE performance for predicting solid and liquid lithium. We also discuss the effect of the index n (in Eq. 6) on cost and accuracy of the results, and compare the performance of a linear ACE (Eq. 3) and a Finnis-Sinclair-type of the energy expansion (Eq. 4).

C. Atomic Cluster Expansion - parametrization

The parameters of the ACE potential are fitted using the Pacemaker package [41–43]. A cut-off of 5.5 Åis chosen for all interactions, based on the range of DFT interactions. From the DFT training data, 10% of the configurations are chosen for validation. For the basis functions, up to 3 body orders in Eq. 8 (4-body interaction terms) are considered. The maximum value of the indices n and l for each order are summarized in Table II. Spherical Bessel-type functions are chosen to expand the radial part of the ACE formalism $(R_{nl}(r_{ji}))$ in Eq. 6),

Solid configurations	Temperature (K)	Volume per ion (\mathring{A}^3)
BCC	0	16.54, 16.60,, 23.53 (100 volumes)
FCC (108 atoms)	0	17.61, 17.66,, 23.24 (100 volumes)
h9R (108 atoms)	0	14.80, 14.90,, 27.02 (100 volumes)
HCP (96 atoms)	0	14.66, 14.75,, 26.76 (100 volumes)
BCC bulk	400	18.01, 19.16, 20.35, 21.60, 22.90
BCC with di-vacancy	400	18.01, 19.16, 20.35, 21.60, 22.90
BCC with tri-vacancy	400	18.01, 19.16, 20.35, 21.60, 22.90
BCC with quad-vacancy	400	18.01, 19.16, 20.35, 21.60, 22.90
BCC with < 111 > SIA	400	16.95, 18.62, 20.40, 22.29
BCC with [100] surface	400	3 volumes (a=2.82 Å, 2.97 Å, 3.12 Å)
BCC with [110] surface (144 atoms)	400	3 volumes (a=2.82 Å, 2.97 Å, 3.12 Å)
FCC bulk (108 atoms)	400	16.88, 18.55, 20.33, 22.21
HCP bulk (144 atoms)	400	16.70, 18.35, 20.10, 21.97
	Temperature (K)	Volume per ion (\mathring{A}^3)
	600	19.62, 20.90, 22.24, 23.62, 25.07
	800	20.90, 22.24, 23.62, 25.07, 26.57
Liquid configurations	1000	20.90, 22.24, 23.62, 25.07, 26.57
	1200	22.24, 23.62, 25.07, 26.57, 28.14
	1400	22.24, 23.62, 25.07, 26.57, 28.14

TABLE I. Summary of the VASP calculations performed for the solid and liquid Li phases to generate configurations for the training dataset. The first four rows are 0 K DFT calculations. The remaining rows are AIMD runs which are performed for 1000 steps in an NVT ensemble at the corresponding volume and temperature. One in every 10 configurations from the AIMD snapshots are chosen for the final training set. The supercell size is 128 atoms unless otherwise mentioned.

which lead to 360 expansion coefficients. With the above chosen values for n, l and k, we end up with 403 basis functions for each cluster expansion $\varphi_i^{(p)}$ in Eq. 5. In total, we train 1166 parameters (360 coefficients for the radial functions, and 403 coefficients for $\varphi_i^{(1)}$ and $\varphi_i^{(2)}$ each). A single-shot fitting to the training data is performed using the BFGS algorithm to obtain the parameters.

In addition, we also train a set of ACE potentials with different cutoffs, body order ν and n_{max} values to study their impact on the solid and liquid properties. Such an analysis is performed to understand the computational cost that comes with choosing a stricter set of initial conditions for training the ACE potential. The details are specified in the Discussion section.

D. Molecular dynamics simulations

All MD calculations in this work are performed using the LAMMPS code [44] with the Performant implementation of the atomic cluster expansion (PACE) library [41–43]. The simulations are done on single-crystal bulk supercells, periodic in all directions, unless otherwise specified. Time integration is performed us-

Fitting input	Value
Cut-off	6 Å
Radial basis function	Spherical Bessel
u-order	1/2/3
n_{max}	15/6/4
l_{max}	0/3/3
Number of parameters (radial part)	360
Number of parameters $c_v^{(1)}$	403
Number of parameters $c_v^{(2)}$	403
Total number of parameters	1166

TABLE II. A summary of details regarding the ACE parametrization used for the results shown in the main text.

ing the velocity-Verlet algorithm [45] with a time-step of 0.5 fs. Temperature and pressure control is done using a Nose-Hoover thermostat [46], and using the Parrinello-Rahman method [47], respectively. Structures are visualized using the OVITO software package [48].

	Energy (meV/atom)	Force (meV/Å)		
	Training	Validation	Training	Validation	
RMSE	1.85	1.71	12.4	12.33	
MAE	0.77	0.78	5.19	5.37	

TABLE III. Summary of the fitting results. The chosen cutoff is 5.5 Å, with up to 4-body interactions and $n_{max} = 15$ as the initial specifications of the ACE potential.

III. RESULTS

A. Fitting results

The root mean square errors (RMSE) and the mean absolute errors (MAE) of the fitted ACE on both the training set and the validation set are provided in Table III. The ACE predicts extremely accurate values of the energies and forces of configurations ($< 2~{\rm meV/atom}$ and $< 13~{\rm meV/Ain}$ error, respectively) from both the training and validation set. We further use the ACE to predict 0 K and high-temperature properties of solid and liquid lithium.

B. Solid lithium

1. 0K phases

The 0 K properties predicted by the ACE potential are compared to corresponding DFT or experimental data, and results using previously existing 2NN-MEAM interatomic potentials for solid lithium from literature. In Table IV, we provide an extensive set of such properties for the fcc, bcc, hcp and h9R phases. Here, we have also compared the DFT results obtained in this work which are calculated as a part of the training set generation. The properties of the h9R phase were not calculated in the literature of the previously existing potentials and are hence left blank.

From the DFT results in Table IV, it is seen that the fcc phase is the lowest-energy ground state structure at 0 K, which has been previously established in literature. The bcc, hcp and h9R are meta-stable phases, but energetically very close to the fcc phase as noticeable from the energy differences. The ACE predicts the fcc phase to have a lower energy than the bcc and hcp phases. The energy difference between the bcc and fcc phase is marginally higher (by 0.0015 eV/atom). However, the ACE predicts the h9R phase to be lower in energy by 0.0001 eV/atom. In addition to the energy differences, the elastic constants predicted by the ACE potential are also in good agreement with DFT for all phases, each of them satisfying the Born criteria [49]. Overall, the ACE

property predictions of the different phases are very satisfying, considering the extremely small energy differences between the different phases. Nonetheless, the bcc phase is known to become entropically stabilized above $\approx 100 \, \mathrm{K}$.

The 0 K energy-volume curve predicted by the ACE in comparison to DFT for the four phases are shown in Fig. 1. Here, the energies are with respect to the equilibrium fcc energy. The hcp and h9R energies are almost exactly reproduced, while the ACE predicts a very marginally higher energy and softer bcc phase by $<0.0015~\rm eV/atom$. This difference might arise from the fact that there are several high-temperature bcc configurations in the training set, driving the ACE towards predicting a slightly softer bcc phase at 0 K.

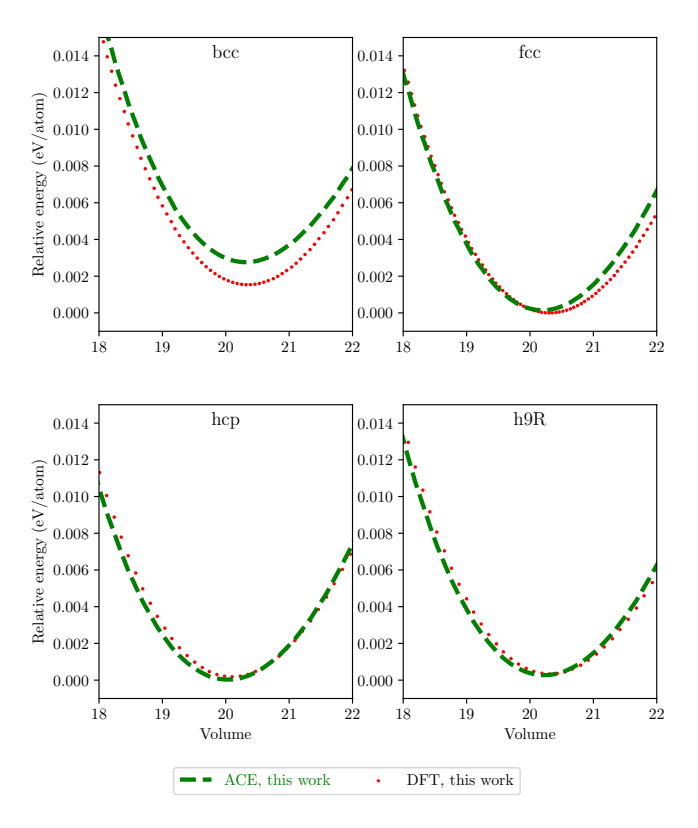


FIG. 1. Energy-volume curves of the four phases with respect to the equilibrium 0 K FCC energy predicted by the ACE potential compared to DFT.

2. Vacancies and Self-interstitial defects

In addition to the $0\,\mathrm{K}$ energies and phase stabilities discussed above, we also validate the $0\,\mathrm{K}$ defect and surface energies predicted by the ACE. We restrict these comparisons only to the experimentally-observed bcc phase. Table V shows the formation energies of a mono-, diand tri-vacancy, six self-interstitial defects, and three different surface energies. The ACE predicts these energies in very good agreement with DFT. The formation of vacancy clusters become increasingly higher in

Structure	Property	DFT (this work)	DFT/Expt. (Literature)	ACE (this work)	MEAM (Literature) [12, 13]
	a	4.331	4.324,4.33	4.328	4.347, 4.298
	Volume	20.3097	20.211,20.309	20.2676	20.536, 19.849
FCC	E_{coh}	-1.61	-1.611	-1.617	-1.63, -1.64
	C_{11}	16.4	16.2	17.3	16.02, 13.45
	C_{12}	12.5	12.5	12.9	12.13, 15.09
	C_{44}	10.1	10.4	11.9	10.92, 10.61
	a	3.439	3.436, 3.44	3.438	3.451, 3.419
	Volume	20.336	20.283,20.354	20.318	20.55, 19.983
BCC	$E-E_{fcc}$	0.0016	0.0015	0.003	0.00054, 0.0015
	C_{11}	14.6	15.0	15.1	16.7, 16.2
	C_{12}	13.7	13.2	13.1	12.6, 13.5
	C_{44}	11.5	11.1	10.7	11.2, 8.6
	a	3.061	3.058	3.06	3.075, 3.033
	c	5.009	5.013	5.007	5.01, 5.015
	Volume	20.3225	20.298	20.301	20.512, 19.976
	$E-E_{fcc}$	0.00019	0.0001	0.0001	0.0005, 0.00074
HCP	C_{11}	26.6	22	24.8	21.1, 14.1
	C_{12}	10.9	11	10.6	12.8, 22.2
	C_{13}	5.2	8	5.8	6.3, 6.4
	C_{33}	32.1	26	30.9	27.6
	C_{44}	7.9	6	7.1	4.4, 2.8
	C_{66}	4.9	6	5.2	
	a	3.06	3.08	3.06	
	c	22.53	22.37	22.26	
	Volume	20.313	20.42	20.057	
	$E-E_{fcc}$	0.00014	0.000	-0.0001	
h9R	C_{11}	19.1	19	20.2	
11316	C_{12}	13.6	14	14.8	
	C_{13}	7.5	8	6.9	
	C_{33}	27.1	27	24.8	
	C_{44}	6.3	5	7.7	
	C_{66}	1.8	2	2.2	
	C_{14}	1.1	1	1.4	

TABLE IV. Properties of Lithium at 0 K in the different energetically competing phases. Current DFT results and ACE predictions are compared to results from literature. The table compares lattice constants a and c (in Å), equilibrium volume (in Å³/atom), the cohesive energy E_{coh} and the energy difference with the FCC phase $E - E_{fcc}$ (in eV/atom), and the elastic constants C_{ij} (in GPa).

energy as observed from the first row. The < 111 > self-interstitial is the lowest-energy interstitial defect in bcc Li. DFT predicts the $\{100\}$ and $\{110\}$ surfaces as the lowest-energy surfaces. The ACE also predicts both these surfaces as the lowest-energy although the $\{110\}$ is lower by $0.001\,\mathrm{eV/atom}$.

3. Temperature-dependent properties

Next, we also use the ACE to calculate temperature-dependent properties of solid Li. Fig. 2 shows the change in lattice constant with temperature predicted by the ACE, in comparison to experiments from literature. The slope of the curve resembles experimental data, although the absolute values are slightly smaller (by around 0.02-

Energy (eV/atom)	Type	DFT (this work)	ACE (this work)	
	Mono-vac	0.457	0.439	
Vacancy	Di-vac	0.952	0.922	
Tormation	Tri-vac	1.397	1.32	
	< 111 >	0.527	0.458	
Self-	< 110 >	0.617	0.581	
interstitial	< 100 >	0.757	0.698	
formation	octahedral	0.81	0.778	
	tetrahedral	0.834	0.838	
Surface	{110}	0.029	0.023	
	{100}	0.027	0.024	
	{111}	0.041	0.044	

TABLE V. Comparison of certain vacancy formation, self-interstitial formation and surface energies of bcc Lithium predicted by the ACE potential to DFT.

0.04Å). The ACE is trained on energies and forces calculated from DFT using the GGA exchange-correlation functional. The GGA functional predicts an over-binding solid, which has been observed in literature for other systems. As a consequence, the ACE also predicts and overbinding solid Li, which leads to slightly smaller values of lattice constant compared to experimentally known values.

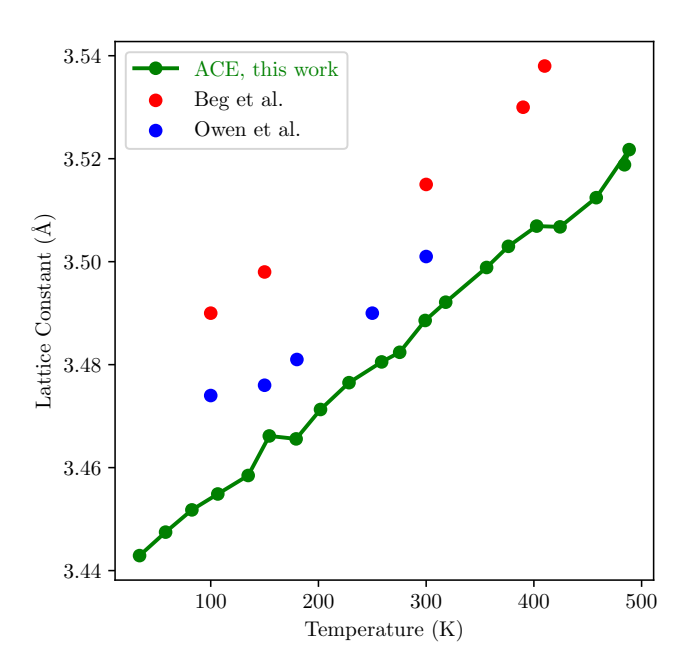


FIG. 2. Lattice constant as a function of temperature for the BCC phase predicted by the ACE potential compared to experimental values.

In Fig. 3, we plot the change in elastic constants (C11, C12 and C14) of the bcc phase predicted by the ACE

compared to experimental data from literature. The slope of the curves are consistent, and the absolute values are accurately predicted by the ACE. All three elastic constants decrease by 3-4 GPa from $0\,\mathrm{K}$ to $400\,\mathrm{K}$, making the bcc solid softer with temperature.

C. Liquid lithium

1. Melting point prediction

The ACE potential, which is trained on solid and liquid configurations, is also used to predict the melting point of Li. In this work, we use the solid-liquid coexistence method to compute the melting point. The MD calculation is performed on a 16,384-atom simulation cell. In the first step, we start with pure bcc Li, and thermally equilibrate the system at the speculated melting point (T_{guess}) (conventionally, we can use the experimental melting point as the initial guess). Next the bottom half of the simulation cell is kept frozen, and the top half is heated from $T_{\rm guess}$ to $2 \times T_{\rm guess}$ in an NPT ensemble, with the cell allowed to relax perpendicular to the plane of separation of the frozen and unfrozen atoms. The above step melts the top half of the cell. We proceed to cool the top half, again in a similar NPT ensemble, from $2 \times T_{\text{guess}}$ back to T_{guess} , which still keeps the top half of the cell melted. As the final step, we release all atoms by relaxing the entire system in an NPH ensemble. If the initial guess is close to the predicted melting point, then the system reaches a temperature while still maintaining an approximately 50-50 coexisting solidliquid phase, and that temperature is the melting point of the system as predicted by the ACE potential. If the initial guess is too high, the entire system melts in the final step, and vice versa. The melting point can be calculated as a function of pressure by following the above procedure, but maintaining the corresponding pressure in the NPT and NPH ensembles.

Figure 4 shows the estimated melting point as a function of pressure predicted by the ACE potential in comparison to an experimental data set from literature. The zero-pressure melting point is predicted as 451 K, very close to the experimental value of 454 K. The ACE potential also replicates increase and eventual tapering of the melting point as a function of pressure. The estimated values are higher by 20 K around 8 GPa. The bcc phase transforms into the fcc phase around 8-10 GPa, further complicating the solid-liquid phase diagram at those pressures, which might be a source of the error in the ACE prediction. Further investigation and an improvement of the training set to include high-pressure structures are needed to understand this discrepancy in more detail.

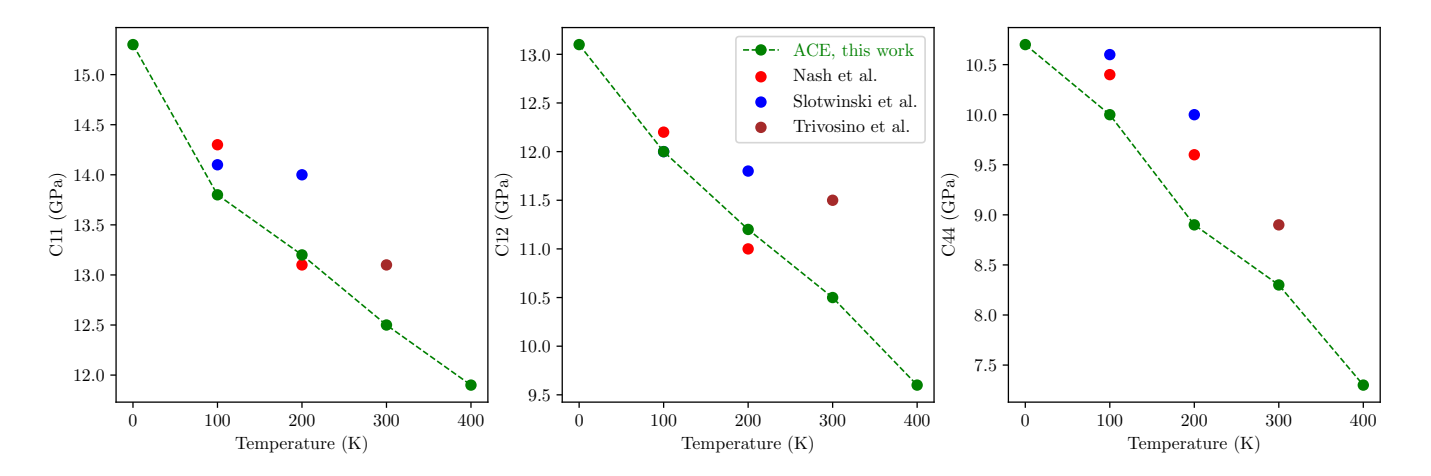


FIG. 3. Elastic constants as a function of temperature for the BCC phase predicted by the ACE potential compared to experimental values.

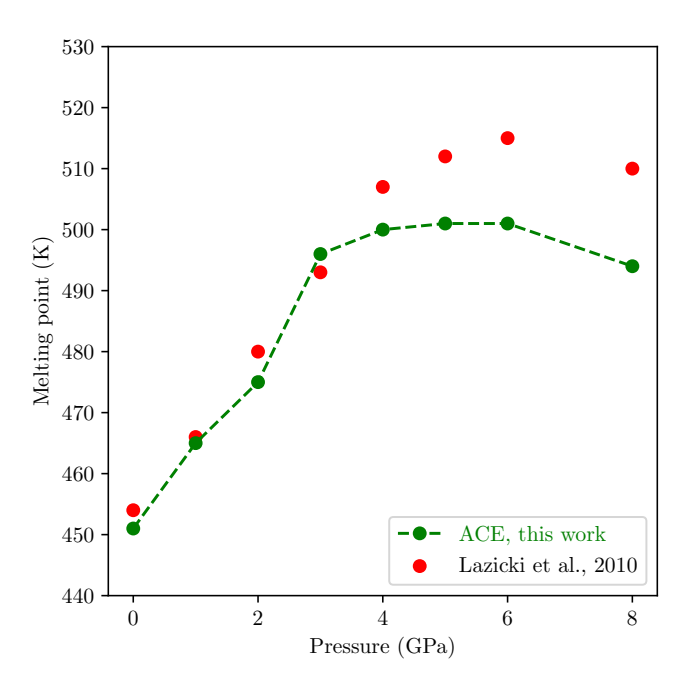


FIG. 4. Change in the predicted melting point by ACE as a function of pressure compared to experimental values.

2. Liquid properties

The results shown for liquid Li have been averaged over MD simulations performed on five different initial liquid structures with different initial random seeds. Figure 5 shows the radial distribution function (RDF) of liquid Li at 868 K predicted very accurately by the ACE potential in comparison to an experimental data set from literature. As expected, the RDF of the liquid phase is smeared out with two gradual peaks close to 3 Åand 5.8 Å.

Figure 6 shows the shear viscosity of liquid Li calcu-

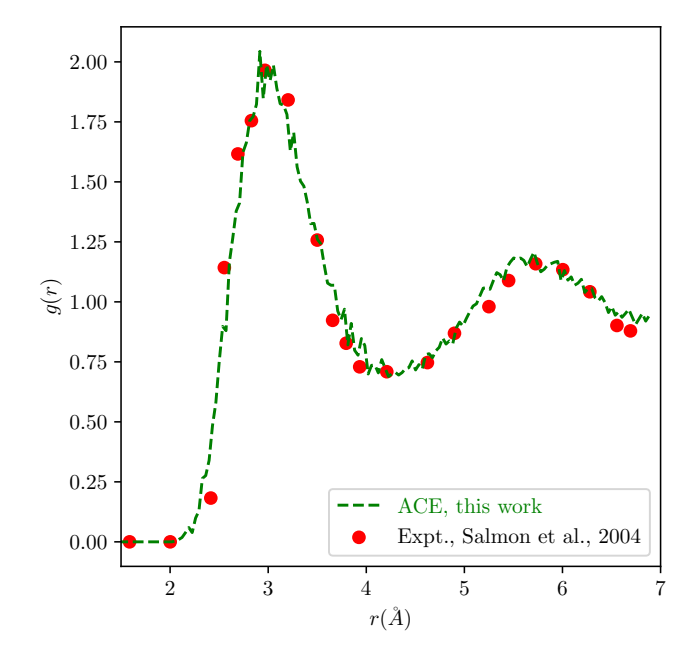


FIG. 5. Radial distribution of liquid Li at $868\,\mathrm{K}$ compared to experimental value from literature.

lated at different temperatures using the ACE, compared to experimental values. The shear viscosity is calculated using the Green-Kubo formalism, given as

$$\eta = \frac{V}{k_B T} \int_{0}^{\infty} dt \left\langle \tau_{\alpha\beta}(t) \tau_{\alpha\beta}(0) \right\rangle_{t_0}$$
 (10)

where V is the system volume, k_B is the Boltzmann constant, T is the temperature, $\tau_{\alpha\beta}$ are off-diagonal components of pressure, t is the time, and $\langle ... \rangle_{t_0}$ is the average over time origins. Time window averages are taken every 1 ps, by considering input values every 2.5 fs and accumulating 400 correlation time windows. The predictions

of the previously developed EAM for liquid Li [19] are also plotted in Fig. 6 for comparison. The ACE predicts a considerable drop in the shear viscosity of liquid Li with temperature, which is also observed experimentally. The absolute values of the viscosity from the ACE potential are closer to experiments than the predictions of the EAM potential.

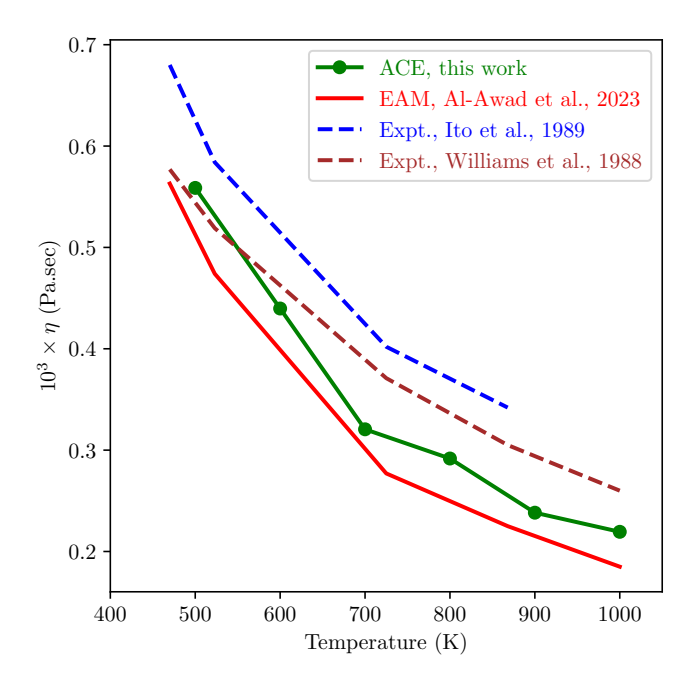


FIG. 6. Shear viscosity of liquid Li at volumes corresponding to that temperature.

The next liquid Li property that we predict and compare is the self-diffusion coefficient D, which is calculated from the mean-squared displacement (MSD), as given as

$$D = \frac{1}{6t} \left\langle (r(t) - r(0))^2 \right\rangle, \tag{11}$$

where r(t) is the position of an atom at time t. The value of D is obtained from the linear part of the MSD-time plot. The self-diffusion coefficients calculated at different temperatures using the ACE potential are plotted in Fig. 7. The values and the trend of the self-diffusion coefficient obtained from the ACE potential fall close to experimental values. For comparison, the EAM-predicted values are also plotted in the same figure.

Lastly, we also plot the liquid densities as a function of temperature in Fig. 8 as predicted by the ACE, in comparison to experiments and EAM. The densities are marginally higher than the experimental values by around 5-15 kg/m³. This can again be attributed to the effect of the over-binding GGA exchange correlation to which the ACE is trained. On the other hand, the EAM was trained to experimental values of the density, which is why the EAM prediction falls exactly on top of the experimental curve. Nonetheless, this does not get translated to other liquid properties that were discussed ear-

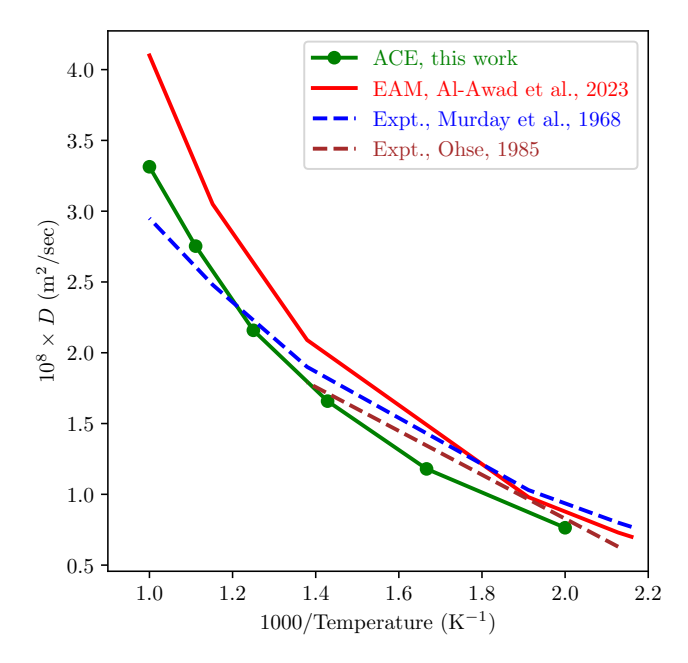


FIG. 7. Self diffusion coefficient of liquid Li at volumes corresponding to that temperature.

lier, where the predictions of the ACE were closer to experimental values. Overall, while the EAM shows a decent performance of predicting liquid properties, the ACE performs even better, while also simultaneously predicting solid Li and the melting points accurately.

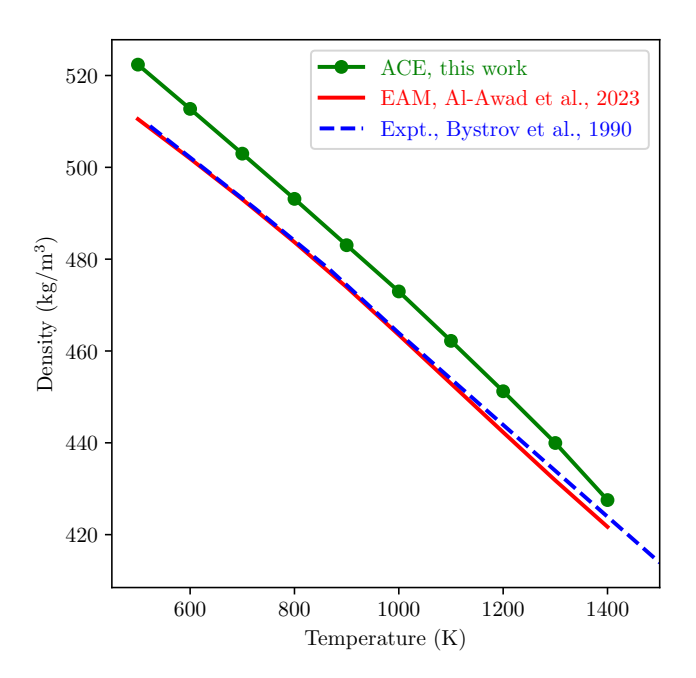


FIG. 8. Atmospheric density of liquid Li.

IV. DISCUSSION

In the previous section, we developed an ACE interatomic potential to predict both solid and liquid lithium properties. The potential included up to 4-body interactions with $n_{max} = 15$ in the expansion of the radial basis, and we imposed a 5.5 Åcut-off on the interatomic interactions in the training set. The performance of the potential was exceptional in predicting both the solid and liquid phase properties and the melting point in comparison to ab initio values. Owing to the large parameter space, the above-developed potential is roughly two orders slower than classical interatomic potentials. Nonetheless, one of the advantages of the ACE formalism is to systematically investigate the effect of higher-body interactions in a model system—in our case, lithium. Since the number of basis functions, and subsequently the cost of performing MD simulations become higher with the inclusion of higher body interactions, it is crucial to find an optimally performing ACE potential for lithium in terms of both computational cost and accuracy.

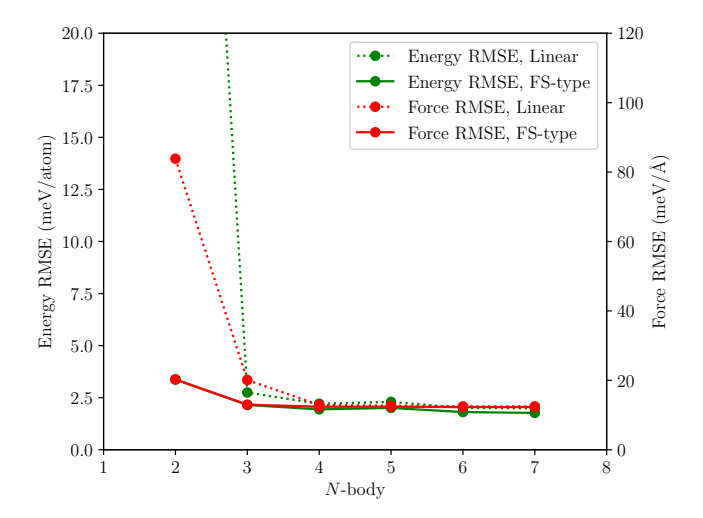


FIG. 9. Root mean squared errors (RMSE) in the energy and atomic forces as a function of the N-body interactions considered in the ACE model. Linear and Finnis-Sinclair type of energy expansion of the ACE formalism are compared.

Figure 9 shows the the RMSE in energies and forces during training of various lithium ACE potentials that included increasing N-body interactions in the ACE basis (Equation 8). The change in the RMSE is shown for ACE potentials of both the linear-type (Equation 3) and the non-linear Finnis-Sinclair-type (Equation 4) formalism. It is observed that the FS-type ACE potential (shown as solid lines in Fig. 9) converges faster in terms of the RMSE, already by including only up to 3-body interactions. This implies that almost all interactions in lithium can be represented by considering only the 2-body and 3-body interactions to the atomic energy

while expanding the energy as a sum of a linear term that signifies pairwise forces, and a square root term that signifies the embedding function. However, if the formalism does not include an explicit embedding-type term, one also needs to consider 4-body interactions before reaching a converged error in the trained energies and forces. The faster convergence of the FS-type formalism can also be explained by its larger parameter space in comparison to the linear-type for the same N-body contributions and training data.

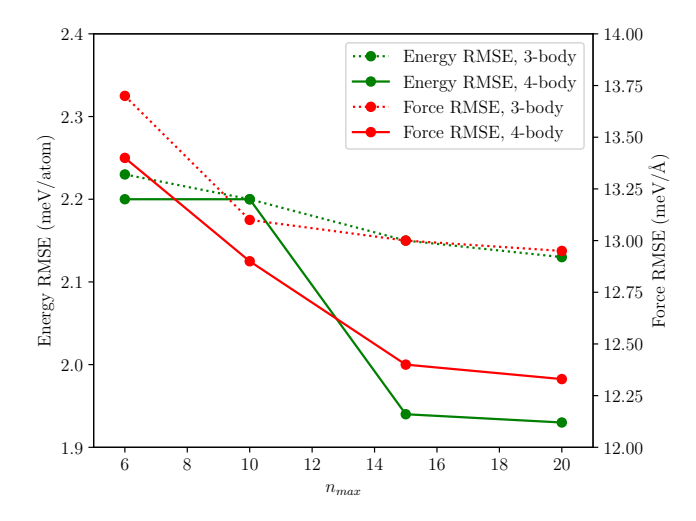


FIG. 10. Root mean squared errors (RMSE) in the energy and forces as a function of n_{max} that is used in the expansion of the radial basis for the 3-body and 4-body interaction ACE models.

In Fig. 10, we show the RMSE in energies and forces of various ACE potentials as a function of n_{max} in the expansion of the radial function (Equation 6). Apart from n_{max} which corresponds to the value of n for the two-body interaction term, the other values of n and l are the same as mentioned in Table 2. The RMSEs are shown only for the FS-type formalism, and while including up to 3-body and 4-body interaction terms in the expansion. The RMSE values converge after a value of $n_{max} = 15$. However, the errors are already very small while having just 6 terms in the expansion of the radial function. While the gain in accuracy is not very significant while going from n = 6 to n = 15, there is a considerable rise in the computational cost (check Table 6) as will be discussed later.

The other parameter in the ACE formalism that affects the performance and computational cost is the cutoff chosen for the interatomic interactions. While a larger cutoff implies a greater accuracy in the atomic energy in the training data, it also implies a larger number energy and force calculations per atom per MD step with the trained potential which increases the computational cost. Figure 11 shows the RMSE in energies and forces of ACE potentials fitted with different cutoffs. In the figure, we only show the case for FS-type ACE potentials including up to 4-body interactions with $n_{max}=15$. The errors are

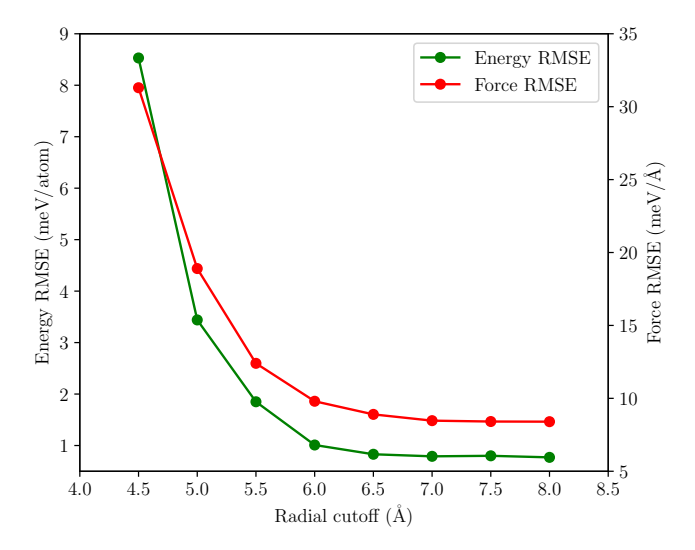


FIG. 11. Root mean squared errors (RMSE) in the energy and forces as a function of the radial cutoff for FS-type formalism ACE potentials with $n_{max}=15$ and up to 4-body interactions.

extremely small (< 2 meV in energy and < 13 meV Åin atomic force) while choosing a 5.5 Åcutoff, and become even smaller and converge to < 0.1 meV in energy at 7 Åalbeit at a higher computational cost.

The above analysis reveals that the RMSE in energy and atomic forces of a trained ACE potential converge to within $2\,\mathrm{meV/atom}$ and $15\,\mathrm{meV/Åfrom}$ ab initio values as long as we choose a non-linear formalism of the ACE potential to include up to 4-body interactions, with an n_{max} value of 15 to expand the radial basis, and a cutoff of 5.5 Å. In fact, to obtain an ACE potential to predict properties of only the liquid phase by training on ab initio MD data of liquid Li (last row in Table 1), expanding the energy to include as much as up to 3-body interactions is sufficient to obtain converged properties of the liquid phase. This has been further discussed in the Supplementary Information.

Including higher body terms is crucial primarily in obtaining the correct 0 K energy differences of the different competing solid phases and the elastic constants of the bcc and the fcc solid. This is evident from Table VI which compares these properties for ACE potentials that were trained with different sets of input conditions to the same DFT training data. Including 4-body interaction terms and choosing a larger n_{max} brings the energy difference between the bcc, hcp and the h9r phases and the fcc phase much more closer to DFT values. A stricter set of parameters is also necessary for obtaining accurate values of the 0 K elastic constants, and especially the correct order of elastic constants (with $C_{11} > C_{12}$) for the bcc phase that satisfies the Born criterion. A significant gain in accuracy is not observed by increasing the cutoff to 7 A. Similarly, adding higher body-order interaction terms above 4 does not further improve the predictions

of the ACE potential.

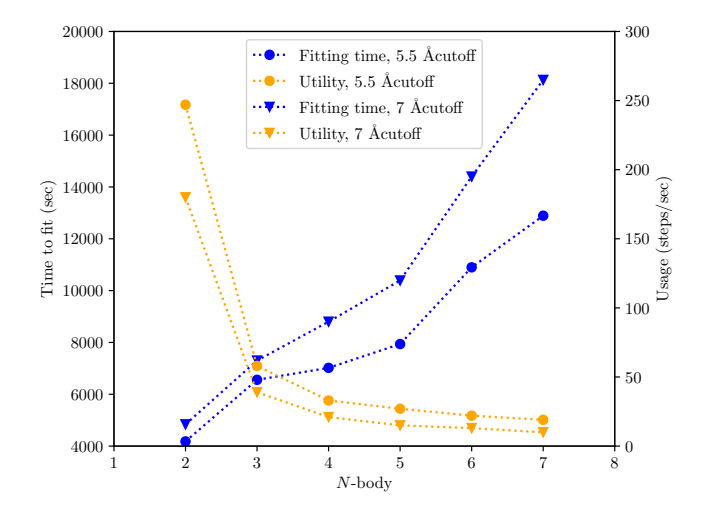


FIG. 12. Time required to fit and the computational cost of doing MD using the ACE as a function of N-body interactions used in the ACE model. The fitting time is measured after 1000 iterations on a single node with 48 CPUs. The usage time is measured as the number of MD steps per second on a 16,384-atom system on a single node with 48 CPUs.

Although considering a higher set of input parameters (body order, n_{max} and cutoff) brings the ACE predictions much closer to DFT, this also significantly increases the computational cost, both for fitting, and more importantly for running MD simulations with the fitted potential. The increase in computational cost for different initial conditions is compared in the last two columns in Table 1. The values are also plotted in Fig. 12 for two specific cases that compares the fitting time and the utility (number of MD steps that can be run per second) as a function of the body order for ACE potentials trained with 5.5 Åand 7 Åcutoff. Both the fitting time and the usage time are a function of the total number of parameters in the ACE potential. The fitting time steadily increases with increase in the body order. By considering an expansion with more than 3-body interaction terms, there is a steady increase in the computational cost of the ACE potential. The ACE potentials trained with a 7 Åcutoff are roughly twice more expensive than the one with 5 Å. Overall, by performing such an analysis, we are able to make an informed decision about the level of the ACE potential that is needed to efficiently model a given system. It is left up to discretion of the MD user to choose a corresponding ACE potential based on the accuracy and the computational cost that one can afford. For the case of Lithium, an ACE potential that predicts both the solid, liquid phases, and melting properties accurately requires initial training specifications as mentioned in Table 2, which has been shown to perform exceptionally in the Results section of this manuscript.

ACE parameters $\Delta E_{\text{bcc-fcc}} \Delta E_{\text{hcp}}$		$\Delta E_{\text{hcp-fcc}} \Delta E_{\text{hgR-fcc}}$		Elastic constants BCC		Elastic constants FCC			Time to fit	Usage	
ACE parameters ΔE_{bcc}	ΔL bcc-fcc	$E_{\rm bcc-fcc} \left \Delta E_{\rm hcp-fcc} \right $	ΔEh9R-fcc	C_{11}	C_{12}	C_{44}	C_{11}	C_{12}	C_{44}	(sec)	(steps/sec)
2-body, 5.5 Å, n=15	0.007	0.0064	0.0015	11.1	12.8	9.9	19.4	13.3	12.1	4180	247
3-body, 5.5 Å, n=15	0.0045	0.0032	0.0029	11.9	12.1	10.9	18.8	13.5	10.9	6558	58
4-body, 5.5 Å, n=6	0.0053	0.0029	0.0022	12.0	12.2	9.7	17.9	11.1	10.1	5099	81
4-body, 5.5 Å, n=10	0.005	0.0033	0.002	12.8	13.1	11.0	17.1	13.4	12.2	6180	69
4-body, 5.5 Å, n=15	0.0036	0.0018	0.001	13.7	13.4	10.0	16.3	14.9	10.9	7019	33
4-body, 7 Å, n=15	0.0026	0.00013	0.0009	15.1	13.9	10.9	16.9	13.1	10.2	8800	21
5-body, 5.5 Å, n=15	0.0034	0.0018	0.0009	13.8	13.1	10.2	16.4	14.7	10.8	7937	27
6-body, 5.5 Å, n=15	0.0035	0.0018	0.0008	13.9	13.2	10.3	16.3	14.5	10.8	10898	22
DFT	0.0016	0.00019	0.00014	14.6	13.7	11.5	16.4	12.5	10.1		

TABLE VI. Comparison of the energy differences of different competing phases in solid Li (in eV) and the 0 K BCC and FCC elastic constants (in GPa) as predicted by ACE potentials fitted with different initial conditions to DFT (last line). In the last two columns, the fitting time and usage time of the potentials are compared. The time to fit is measured after 1000 iterations on a single node with 48 CPUs. The usage time is measured as the number of LAMMPS MD steps per second on a 16,384 atom system on a single node with 48 CPUS.

V. CONCLUSIONS

In this work, we have developed an atomic cluster expansion interatomic potential for lithium. The potential predicts accurate properties of both the solid and liquid phase, and an accurate melting point in comparison to ab initio data and experiments, respectively. We have performed an extensive cost-accuracy analysis by training several potentials using the ACE formalism. Most of the interactions in lithium can be captured by expanding the energy using 3-body terms. Hence, a relatively computationally cheaper 3-body expanded ACE potential is sufficient to model liquid lithium. However, including 4-body interactions in the ACE expansion is absolutely

crucial in capturing the correct 0 K energies and elastic constants of different competing phases in solid Li.

ACKNOWLEDGMENTS

This project was funded by UKAEA through the Department for Science, Innovation and Technology's International Science Partnership Fund (ISPF). DNM and PS would like to thank the EUROfusion for providing Fusion HPC facilities on Marconi and Leonardo machines in generation of the DFT data used for this paper. PS, MRG and DNM also acknowledge funding by the EPSRC Energy Programme (EP/W006839/1).

I. Kirillov, I. Danilov, S. Sidorenkov, Y. Strebkov, R. Mattas, Y. Gohar, T. Hua, and D. Smith, Liquid lithium self-cooled breeding blanket design for iter, Fusion Engineering and Design 39-40, 669 (1998).

^[2] S. Konishi, M. Enoeda, M. Nakamichi, T. Hoshino, A. Ying, S. Sharafat, and S. Smolentsev, Functional materials for breeding blankets—status and developments, Nuclear Fusion 57, 092014 (2017).

^[3] S. Malang and R. Mattas, Comparison of lithium and the eutectic lead-lithium alloy, two candidate liquid metal breeder materials for self-cooled blankets, Fusion Engineering and Design 27, 399 (1995), proceedings of the Third International Symposium on Fusion Nuclear Technology.

^[4] C. L. Guillaume, E. Gregoryanz, O. Degtyareva, M. I. McMahon, M. Hanfland, S. Evans, M. Guthrie, S. V. Sinogeikin, and H.-K. Mao, Cold melting and solid structures of dense lithium, Nature Physics 937, 211 (2011).

^[5] I. Tamblyn, J.-Y. Raty, and S. A. Bonev, Tetrahedral

clustering in molten lithium under pressure, Phys. Rev. Lett. **101**, 075703 (2008).

^[6] M. Hanfland, K. Syassen, N. E. Christensen, and D. L. Novikov, New high-pressure phases of lithium, Nature 408, 174 (2000).

^[7] G. J. Ackland, M. Dunuwille, M. Martinez-Canales, I. Loa, R. Zhang, S. Sinogeikin, W. Cai, and S. Deemyad, Quantum and isotope effects in lithium metal, Science 356, 1254 (2017).

^[8] M. Hutcheon and R. Needs, Structural and vibrational properties of lithium under ambient conditions within density functional theory, Physical Review B 99, 10.1103/PhysRevB.99.014111 (2019).

^[9] S. S. Behara, J. Thomas, and A. Van der Ven, Fundamental thermodynamic, kinetic, and mechanical properties of lithium and its alloys, Chemistry of Materials 36, 7370 (2024).

^[10] S. S. Behara, J. Thomas, and A. Van der Ven, Fundamental thermodynamic, kinetic, and mechanical properties of

- lithium and its alloys, Chemistry of Materials **36**, 7370 (2024).
- [11] A. Nichol and G. J. Ackland, Property trends in simple metals: An empirical potential approach, Phys. Rev. B 93, 184101 (2016).
- [12] W. S. Ko and J. B. Jeon, Interatomic potential that describes martensitic phase transformations in pure lithium, Computational Materials Science 129, 202 (2017).
- [13] Meam interatomic potential for thermodynamic and mechanical properties of lithium allotropes, Computational Materials Science 214, 10.1016/j.commatsci.2022.111706 (2022).
- [14] Accurate surface and finite-temperature bulk properties of lithium metal at large scales using machine learning interaction potentials, ACS Omega 9, 10904 (2024).
- [15] Y. Zuo, C. Chen, X. Li, Z. Deng, Y. Chen, J. Behler, G. Csányi, A. V. Shapeev, A. P. Thompson, M. A. Wood, and S. P. Ong, Performance and cost assessment of machine learning interatomic potentials, The Journal of Physical Chemistry A 124, 731 (2020), pMID: 31916773.
- [16] X. Wang, Z. Wang, P. Gao, C. Zhang, J. Lv, H. Wang, H. Liu, Y. Wang, and Y. Ma, Data-driven prediction of complex crystal structures of dense lithium, Nature Communications 14, 10.1038/s41467-023-38650-y (2023).
- [17] Application of the embedded atom model to liquid metals: Liquid lithium, High Temperature 47, 211 (2009).
- [18] Z. Cui, F. Gao, Z. Cui, and J. Qu, Developing a second nearest-neighbor modified embedded atom method interatomic potential for lithium, Modelling and Simulation in Materials Science and Engineering 20, 015014 (2011).
- [19] A. S. Al-Awad, L. Batet, and L. Sedano, Parametrization of embedded-atom method potential for liquid lithium and lead-lithium eutectic alloy, Journal of Nuclear Materials 587, 154735 (2023).
- [20] N. Artrith, A. Urban, and G. Ceder, Efficient and accurate machine-learning interpolation of atomic energies in compositions with many species, Phys. Rev. B 96, 014112 (2017).
- [21] A. P. Bartók, M. C. Payne, R. Kondor, and G. Csányi, Gaussian approximation potentials: The accuracy of quantum mechanics, without the electrons, Phys. Rev. Lett. 104, 136403 (2010).
- [22] J. Behler and M. Parrinello, Generalized neural-network representation of high-dimensional potential-energy surfaces, Phys. Rev. Lett. 98, 146401 (2007).
- [23] A. Thompson, L. Swiler, C. Trott, S. Foiles, and G. Tucker, Spectral neighbor analysis method for automated generation of quantum-accurate interatomic potentials, Journal of Computational Physics 285, 316 (2015).
- [24] Z. Li, J. R. Kermode, and A. De Vita, Molecular dynamics with on-the-fly machine learning of quantummechanical forces, Phys. Rev. Lett. 114, 096405 (2015).
- [25] F. C. Mocanu, K. Konstantinou, T. H. Lee, N. Bernstein, V. L. Deringer, G. Csányi, and S. R. Elliott, Modeling the phase-change memory material, ge2sb2te5, with a machine-learned interatomic potential, The Journal of Physical Chemistry B 122, 8998 (2018), pMID: 30173522.
- [26] M. Rupp, A. Tkatchenko, K.-R. Müller, and O. A. von Lilienfeld, Fast and accurate modeling of molecular atomization energies with machine learning, Phys. Rev. Lett. 108, 058301 (2012).

- [27] S. Manzhos and J. Carrington, Tucker, A random-sampling high dimensional model representation neural network for building potential energy surfaces, The Journal of Chemical Physics 125, 084109 (2006).
- [28] A. V. Shapeev, Moment tensor potentials: A class of systematically improvable interatomic potentials, Multiscale Modeling & Simulation 14, 1153 (2016).
- [29] A. Takahashi, A. Seko, and I. Tanaka, Conceptual and practical bases for the high accuracy of machine learning interatomic potentials: Application to elemental titanium, Phys. Rev. Mater. 1, 063801 (2017).
- [30] M. A. Wood and A. P. Thompson, Extending the accuracy of the SNAP interatomic potential form, The Journal of Chemical Physics 148, 241721 (2018).
- [31] R. Drautz, Atomic cluster expansion for accurate and transferable interatomic potentials, Physical Review B 99, 014104 (2019).
- [32] J. Nigam, S. N. Pozdnyakov, K. K. Huguenin-Dumittan, and M. Ceriotti, Completeness of atomic structure representations, APL Machine Learning 2, 016110 (2024).
- [33] G. Dusson, M. Bachmayr, G. Csányi, R. Drautz, S. Etter, C. van der Oord, and C. Ortner, Atomic cluster expansion: Completeness, efficiency and stability, Journal of Computational Physics 454, 110946 (2022).
- [34] G. Kresse and J. Hafner, Ab initio molecular-dynamics simulation of the liquid-metal-amorphous-semiconductor transition in germanium, Phys Rev B 49 (1994).
- [35] P. E. Blöchl, Projector augmented-wave method, Phys. Rev. B 50, 17953 (1994).
- [36] G. Kresse and J. Furthmüller, Efficient iterative schemes for ab initio total-energy calculations using a plane-wave basis set, Phys Rev B 54 (1996).
- [37] J. P. Perdew, K. Burke, and M. Ernzerhof, Generalized gradient approximation made simple, Phys. Rev. Lett. 77, 3865 (1996).
- [38] D. M. Ceperley and B. J. Alder, Ground state of the electron gas by a stochastic method, Phys. Rev. Lett. 45, 566 (1980).
- [39] M. Methfessel and A. T. Paxton, High-precision sampling for Brillouin-zone integration in metals, Phys. Rev. B 40, 3616 (1989).
- [40] M. Finnis and J. Sinclair, A simple empirical n-body potential for transition metals, Philosophical Magazine A 50, 45 (1984).
- [41] Y. Lysogorskiy, C. v. d. Oord, A. Bochkarev, S. Menon, M. Rinaldi, T. Hammerschmidt, M. Mrovec, A. Thompson, G. Csányi, C. Ortner, et al., Performant implementation of the atomic cluster expansion (pace) and application to copper and silicon, npj Computational Materials 7, 1 (2021).
- [42] A. Bochkarev, Y. Lysogorskiy, S. Menon, M. Qamar, M. Mrovec, and R. Drautz, Efficient parametrization of the atomic cluster expansion, Physical Review Materials 6, 013804 (2022).
- [43] Y. Lysogorskiy, A. Bochkarev, M. Mrovec, and R. Drautz, Active learning strategies for atomic cluster expansion models, Physical Review Materials 7, 043801 (2023).
- [44] S. J. Plimpton, Fast parallel algorithms for short-range molecular dynamics, Journal of Computer Physics 117, 1 (1995).
- [45] W. Swope, H. Anderson, P. Berens, and K. Wilson, A computer simulation method for the calculation of equilibrium constants for the formation of physical clusters of

- molecules: Application to small water clusters, Journal of Chemical Physics **76**, 637 (1982).
- [46] S. Nose, A unified formulation of the constant temperature molecular-dynamics methods, Journal of Chemical Physics 81, 511 (1984).
- [47] M. Parrinello and A. Rahman, Polymorphic transitions in single crystals: A new molecular dynamics method, Journal of Applied Physics 52,
- 7182 (1981), https://pubs.aip.org/aip/jap/article-pdf/52/12/7182/18394754/7182_1_online.pdf.
- [48] A. Stukowski, Visualization and analysis of atomistic simulation data with OVITO-the open visualization tool, Modeling and Simulation in Materials Science and Engineering 18 (2010).
- [49] F. Mouhat and F. m. c.-X. Coudert, Necessary and sufficient elastic stability conditions in various crystal systems, Phys. Rev. B 90, 224104 (2014).